Experimental and Numerical Study of Mixing Behavior inside Droplets in Microchannels

Wentan Wang, Ting Shao, Shufang Zhao, Yong Jin, and Yi Cheng
Dept. of Chemical Engineering, Tsinghua University, Beijing 100084, P.R. China

DOI 10.1002/aic.13945

For the practical applications of droplet-based microfluidics, we have paid special attention to the complex hydrodynamics and mixing performance inside microdroplets and the profound process intensification when forcing the droplets to move in winding channels. In this work, experimental studies using micro laser induced fluorescence (μ-LIF) technique and three-dimensional simulation based on a multiphase, multicomponents lattice Boltzmann model approach were adopted. The simulation results clearly revealed that the mixing inside the droplet is due to the convection in symmetric vortices in the two hemispheres of the droplet and the diffusion between them. They also showed the fluids inside the droplet could be reoriented due to the winding effect. Three designs of winding channels were studied, where interesting results showed the similar effect of process intensification by breaking up the flow symmetry. The revealed flow mechanism and the mixing performance inside the droplet in droplet-based microfluidics should be helpful for microdevice design and optimization.
AIChE J, 59: 1801–1813, 2013
Keywords: microfluidics, multiphase flow, mixing, microdroplet, lattice Boltzmann method

Introduction

Using microdroplets as individual nanovolume batch reactors becomes very promising in practical applications. For example, droplet-based microfluidics can help to enhance and accelerate cell encapsulation,[1] protein crystallization,[2] enzymatic kinetics,[3] drug delivery,[4] and so on. Meanwhile, the precise control on the underlying hydrodynamics and processes by the droplets in microfluidic devices leads to new scientific methods and insights.[5] Accordingly, growing interest has been put in this fascinating area dominated by the microhydrodynamics of droplets.

With downscaling of the channel size, the viscous and interfacial forces in microfluidics system become more and more predominant. The flows generally remain laminar under very low Reynolds numbers and hardly change to turbulent. Therefore, mixing and chemical reactions occur mainly by molecular diffusion, which is usually too slow, even at the scale of microfluidic devices. Some researchers have tried to enhance the mixing and the reactions using chaotic advection,[6–10] where the droplet-based microfluidics is one of the means to implement the process intensification. It has been noticed that chaotic advection inside a droplet has the special feature of precisely controlling little amount of liquid with a narrow residence time distribution.[11] Besides the droplets in a microchannel, the mixing process in hanging droplets out of a microchannel outlet is also one of the droplet-based mixing methods for process intensification.[12] Understanding the flow phenomenon inside a droplet is, therefore, of great significance for fluid handling in droplet-based microfluidic systems.

Both experiments and lattice Boltzmann simulations were carried out to study the gas–liquid flow in microchannels under various conditions.[13] The flow regimes with different bubble shapes were found depending on the capillary number of the fluid flow. A volumetric velocity distribution inside a droplet was measured by the confocal micro particle image velocimetry (μ-PIV) technique. The results suggested that a three-dimensional (3-D) complex circulating flow existed inside the droplet.[14] The measured velocity fields by micro-PIV were compared with the simulation results obtained by an interface-capturing technique without any interface reconstruction.[15] 2-D simulations were carried out to calculate the concentration field of a chemical component in a square microchannel by means of volume-of-fluid method.[16] Both the experiments and the simulations revealed some flow mechanisms in the droplet-based microfluidics. However, because of complexity in physics and measurement technique constraints, the flow phenomena, especially the mixing behaviors of different components inside a droplet, are still not very clear.

In the present study, the multicomponent lattice Boltzmann model (LBM) proposed by Shan and Chen[17] was further developed for the two-phase flow simulation in microfluidic devices. 3-D simulations based on LBM were performed with a reasonable computational cost. Special attention was paid to the determination of mixing behaviors inside the moving droplet in microchannels. Here, both straight and winding channels were investigated to see different flow patterns inside the microdroplets.

Correspondence concerning this article should be addressed to Y. Cheng at yicheng@tsinghua.edu.cn.

Experimental Setup

Microfluidic devices and materials

Figure 1a shows the schematic diagram of the laser induced fluorescence (μ-LIF) experimental system. A 1.5-W diode pumped solid state continuous laser with a 532-nm characteristic wave length was set to lightening the flow field from the underneath of the microchannel plate. The images of the lighted flow fields were captured at a frequency of 200 frames s^{-1} by a 12-bit CCD camera (IMPERX, IPX-VGA210-L, USA), fixed on top of the microscope. The corresponding spatial resolution was 5 μm pix^{-1}. A high-pass optical filter in front of the camera filtered the scattered and reflected laser to ensure that only the fluorescence signal was received by the camera. Rhodamine B was chosen as the fluorescent tracer. The averaged fluorescence intensity (in terms

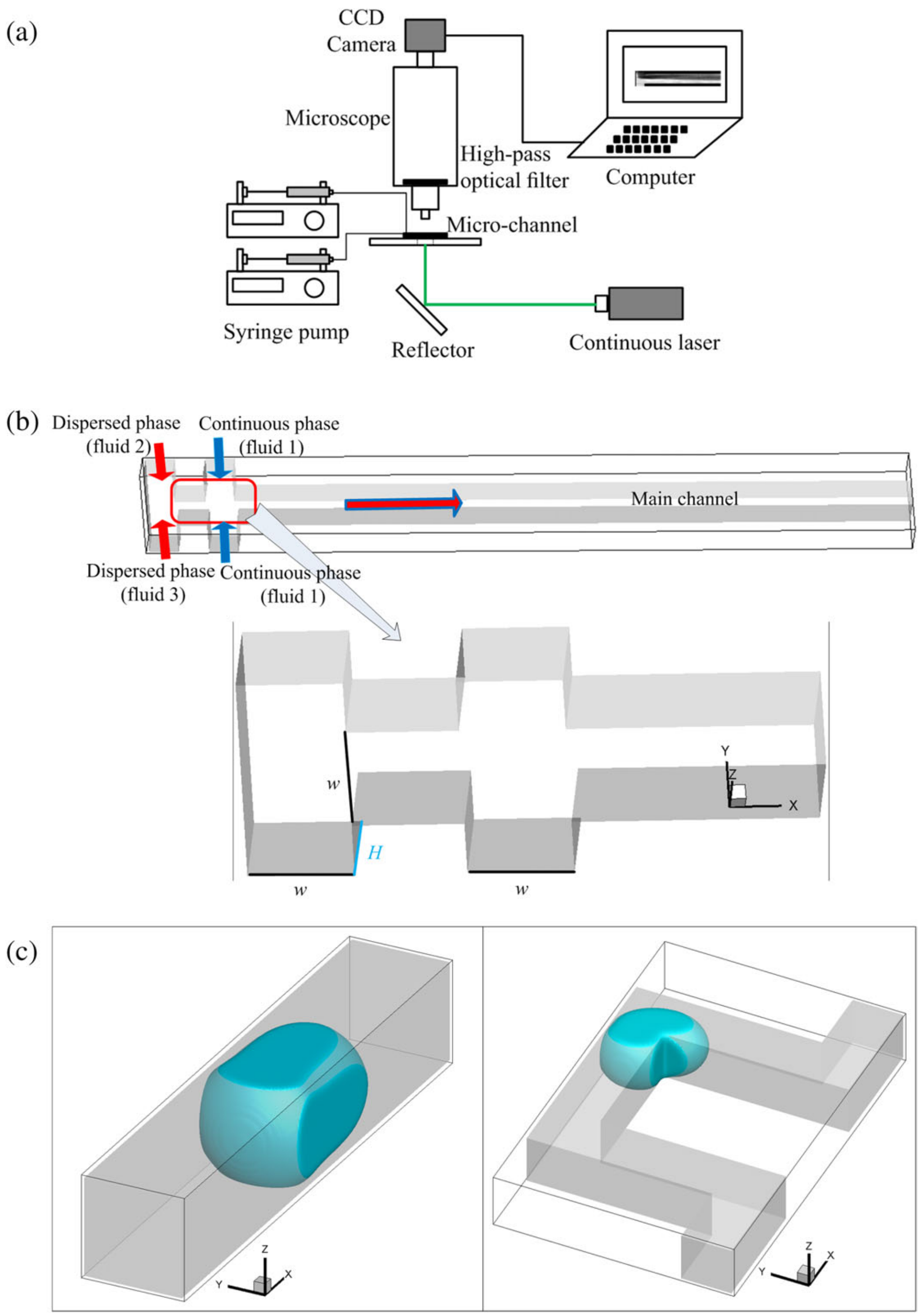

Figure 1. (a) A schematic diagram of experimental system.

(b) The structure of the cross-shaped microchannel. Simulation: $w = 20$ lattice, $H = 20$ lattice; Experiment: $w = 200$ μm, $H = 200$ μm. (c) The structure of the straight and 90°-winding microchannels. [Color figure can be viewed in the online issue, which is available at wileyonlinelibrary.com.]

of gray value) in the z direction was collected by the camera. In this way, some mixing details of the cross-section along the channel would be lost, but the extent of mixing process could still be captured through the 2-D measurements.

As shown in Figure 1b, the cross-shaped microchannel used in the experiments was fabricated on a polymethyl methacrylate (PMMA) sample plate by precise milling and sealed with a thin PMMA cover slide using low azeotropic solvent method.[18] Two syringe pumps were used to pump the liquids into the microchannel device, where deionized water was injected as the disperse phase, while the n-octane with 0.5 wt % Span80 was injected as the continuous phase. The contact angle of the water in this case was 160°, and the viscosity ratio (μ_c/μ_d) was 0.5. Rhodamine B (absorption spectrum 460−590 nm, max = 550 nm; emission spectrum 550−680 nm, max = 590 nm) was u as the fluorescent tracer. Figure 1c shows the geometry of the straight and winding channels used in simulation, and the detail information will be given in section The computational domain.

Calibration of μ-LIF experiment

To measure the concentration field in the mixing channel, one inlet stream contains the Rhodamine B as the fluorescent tracer. The fluorescence intensity (I_C) is proportional to the concentration (C) of Rhodamine B in the dilute solution,[19,20] as shown in Eq. 1

$$I_C = \Gamma_1 \cdot C \cdot \exp(-\Gamma_2 \cdot C) \tag{1}$$

where Γ_1 is the local coefficient related to the experimental parameters; Γ_2 is the coefficient that takes into account the effect of absorption. Under the condition of small concentrations of the tracer, the fluorescence intensity is linearly dependent on the concentration of Rhodamine B. The calibration experiments were carried out *in situ* in the experimental system. First, six solutions of Rhodamine B at different concentrations were prepared accurately. Then, the laser, camera, and microchannel chip were adjusted to the proper positions, exactly the same as in the subsequent experiments. Some parameter settings, such as the laser energy, diaphragm, and exposure time were also fixed. By plotting the average fluorescence intensity (Gray value) vs. the tracer concentration (C), the calibration curve was obtained.[12,21,22]

Mathematical Model of LBM

LBM is a relatively new method for fluid flow simulations. Its origin could be traced to the lattice gas cellular automata. The basic governing equations of LBM can be obtained by discretizing the Boltzmann equation in both temporal and spatial dimensions. In contrast to the conventional computational fluid dynamics method, LBM is positioned between the continuum level described by the Navier–Stokes equation and the microscopic (molecular) level, which is suitable for modeling processes at the mesoscale, such as fluid flows in microchannels. The governing equations of LBM can be conveniently expanded to simulate multiphase fluids. One of the advantages of LBM for multiphase flows is that the phase separation of two immiscible fluid components takes place spontaneously, without the need to track the interface. It is also convenient to control the wettability of the solid surface for the fluid components. Several approaches for multiple component and multiphase flow, such as the chromodynamic,[23] the interaction potential[17] and the free-energy,[24] have been developed in the framework of LBM. Each of these formulations has its own drawbacks: the coloring and recoloring step of chromodynamic are complex and time-consuming; the interaction potential approach has some spurious current at the interface region and the model works well for low density ratios only; and the free-energy approach suffers from the lack of Galilean invariance. Although there are disadvantages for each approach, they are still widely used to simulate multiphase and multicomponent flows in the microfluidic systems.[13,25–27]

Multicomponent LB model

In the modeling scheme of LBM, the fluids are assumed to be composed of packs of virtual fluid particles streaming and colliding along certain lattice directions. Probability density functions (PDFs) are used to describe the motion behaviors of these fluid particles and the macroproperties of fluids, such as velocity, pressure, and density, can be statistically calculated. Among different LB methods, the lattice Boltzmann Bhatnagar-Gross-Krook (BGK) model is considered as the most robust.[28] In the BGK model, a single parameter relaxation term is used to act as the fluid particle collision process. In this work, we used the interaction potential approach for its ease of implementation and the isotropic nature of solutions and further developed the multicomponent LB model proposed by Shan and Chen for three-component flow simulation in microfluidic devices.[17,29]

To simulate the three-component flow processes, three sets of PDFs should be introduced. The script σ denotes the different fluid components by specifying $\sigma = 1$, 2, or 3, and $\bar{\sigma}$ indicates one of the other fluid components. The evolution of the particle distribution is described by Eq. 2

$$f_{\sigma\mathrm{i}}(\boldsymbol{x}+\boldsymbol{e}_\mathrm{i}\delta t, t+\delta t) = f_{\sigma\mathrm{i}}(\boldsymbol{x},t) - \frac{1}{\tau_\sigma}\left[f_{\sigma\mathrm{i}}(\boldsymbol{x},t) - f_{\sigma\mathrm{i}}^{\mathrm{eq}}(\boldsymbol{x},t)\right] \tag{2}$$

In the simplest implementation, with $\delta x = 1$, $\delta t = 1$, the equilibrium function is expressed as

$$f_{\sigma\mathrm{i}}^{\mathrm{eq}}(\boldsymbol{x}) = w_\mathrm{i}\rho_\sigma(\boldsymbol{x})\left[1 + \frac{\boldsymbol{e}_i \cdot \boldsymbol{u}_\sigma^{\mathrm{eq}}}{c_\mathrm{s}^2} + \frac{(\boldsymbol{e}_i \cdot \boldsymbol{u}_\sigma^{\mathrm{eq}})^2}{2c_\mathrm{s}^4} - \frac{\boldsymbol{u}_\sigma^{\mathrm{eq}2}}{2c_\mathrm{s}^2}\right] \tag{3}$$

where w_i is the weight coefficient, $\boldsymbol{u}_{\mathrm{eq}}$ is the equilibrium velocity, $\boldsymbol{e}_\mathrm{i}$ is the discrete velocity associated with the *i-th* lattice direction, τ_σ is the relaxation time, which determines the kinematics viscosities of these three fluids, and c_s is the lattice sound speed. In the D3Q19 lattice (19 velocity vectors in 3-D), the value of c_s is equal to $\sqrt{3}/3$. The weight coefficient values of the D3Q19 lattice are given in Eq. 4.

$$w_0 = \frac{1}{3},\ w_{1-6} = \frac{1}{18},\ w_{7-18} = \frac{1}{36} \tag{4}$$

These evolution equations are linked to each other by using a force term contained in the equilibrium velocity $\boldsymbol{u}_\sigma^{\mathrm{eq}}$, as shown in Eq. 5

$$\boldsymbol{u}_\sigma^{\mathrm{eq}} = \boldsymbol{u}' + \frac{\tau_\sigma}{\rho_\sigma}F_\sigma \tag{5}$$

The equilibrium velocity $\boldsymbol{u}_\sigma^{\mathrm{eq}}$ is computed from a composite macroscopic velocity $\boldsymbol{u}'$.

$$\boldsymbol{u}' = \frac{\sum_\sigma \rho_\sigma/\tau_\sigma \boldsymbol{u}_\sigma}{\sum_\sigma \rho_\sigma/\tau_\sigma} \tag{6}$$

which differs from the macroscopic uncoupled velocities $\boldsymbol{u}_\sigma$ of the individual fluids.

$$\boldsymbol{u}_{\text{sigma}}(\boldsymbol{x}, t) = \frac{1}{\rho_\sigma} \sum_{\text{i}} \boldsymbol{e}_{\text{i}} \sigma_{\text{i}}(\boldsymbol{x}, t) \tag{7}$$

The density for each component is as usual

$$\rho_\sigma(\boldsymbol{x}, t) = \sum_i \sigma_i(\boldsymbol{x}, t) \tag{8}$$

The force F_σ is a sum of two force terms, as shown in Eq. 9. These two forces are the interaction force between different fluid components, denoted by F_σ^{P}, and the interaction force between fluids and the solid surface, denoted by F_σ^{s}.

$$F_\sigma = F_\sigma^P + F_\sigma^s \tag{9}$$

$$F_\sigma^P = -\psi_\sigma(\boldsymbol{x}) \sum_\sigma G_{\sigma\bar{\sigma}} \sum_i w_i \psi_{\bar{\sigma}}(\boldsymbol{x} + \boldsymbol{e}_{\text{i}}) \cdot \boldsymbol{e}_{\text{i}} \tag{10}$$

$$F_\sigma^{\text{s}} = -\psi_\sigma \boldsymbol{x} \sum_i G_{\sigma\text{s}} w_{\text{i}} s(\boldsymbol{x} + \boldsymbol{e}_{\text{i}}) \cdot \boldsymbol{e}_{\text{i}} \tag{11}$$

where $\psi_\sigma(x)$ is the interaction potential of the component σ

$$\psi_\sigma = \rho_{\sigma 0}[1 - \exp(-\rho_\sigma/\rho_{\sigma 0})] \tag{12}$$

$\rho_{\sigma 0}$ is an arbitrary constant. $G_{\sigma\bar{\sigma}}$ is the interaction strength between different fluid particles. By adjusting the value of $G_{\sigma\bar{\sigma}}$ among the components (σ = 1, 2, and 3), we can get the miscible and immiscible fluids among these three components. The relative value of $G_{\sigma\bar{\sigma}}$ also determines the diffusion speed between the miscible components. The parameter $G_{\sigma s}$ is the interaction strength between the solid and the fluid component σ. The variable $s(x)$ equals to 1, if x is in solid and to 0, if x is in fluid. The relative value of $G_{\sigma s}$ between each component determines the wetting conditions of these components on the solid surface. The macroproperties of fluids, that is, density ρ, velocity U, kinematics viscosities v, and pressure p, can be calculated by Eqs. 13–16, respectively.

$$\rho(\boldsymbol{x}, t) = \sum_\sigma \rho_\sigma \tag{13}$$

$$\rho(\boldsymbol{x}, t)\boldsymbol{U}(\boldsymbol{x}, t) = \sum_\sigma \sum_{\text{i}} \boldsymbol{e}_{\text{i}} \sigma_{\text{i}}(\boldsymbol{x}, t) + \frac{1}{2} \sum_\sigma F_\sigma(\boldsymbol{x}, t) \tag{14}$$

$$v_\sigma = \frac{1}{3}\left(\tau_\sigma - \frac{1}{2}\right) \tag{15}$$

$$p(\boldsymbol{x}, t) = c_{\text{S}}^2 \sum_\sigma \rho_\sigma(\boldsymbol{x}, t) + \frac{1}{2} c_{\text{S}}^2 \sum_{\sigma\bar{\sigma}} G_{\sigma\bar{\sigma}} \psi_\sigma(\boldsymbol{x}, t) \psi_{\bar{\sigma}}(\boldsymbol{x}, t) \tag{16}$$

Boundary conditions

The "mid-plane" bounce-back scheme[30] is used to realize a nonslip wall boundary condition. There are two kinds of boundary conditions used for the inlet and outlet boundaries. One is the nonequilibrium bounce-back scheme: the velocity of each component is given at the inlet boundaries, while the pressure is held constant at the outlet boundary. The original algorithm was developed by Zou and He.[31] In the other scheme, a modified periodic boundary condition is set when reaching for the steady state. The algorithm was developed by Zhang and Kwok.[32] To simulate the multicomponents, the average pressure is used instead of the average density, as shown in Eq. 17.

$$f_{\sigma\text{inlet}}^{\text{in}} = f_{\sigma\text{outlet}}^{\text{out}} \frac{p_0 + \beta}{\bar{p}_{\text{outlet}}}, \; f_{\sigma\text{outlet}}^{\text{in}} = f_{\sigma\text{inlet}}^{\text{out}} \frac{p_0 - \beta L}{\bar{p}_{\text{inlet}}} \tag{17}$$

where L is the channel length along the moving direction for periodicity, β is a constant representing the overall pressure gradient along the periodic direction, and $\bar{p}_{\text{inlet}}$ and $\bar{p}_{\text{outlet}}$ are the average pressures over the inlet and the outlet, respectively.

The computational domain

In our simulations, the computational domain is 3-D meshed by square grids. Dimensionless variables are used in all the simulation cases. The velocity field inside the droplet moving in a straight channel is first studied with a computational domain consisting of 200 × 40 × 40 lattices, as shown in Figure 1c. Then, the flow patterns inside the droplets in the winding channels are investigated with a computational domain consisting of 200 × 90 × 22 lattices (e.g., for the 90°-winding channel shown in Figure 1c). The channel width (or the depth) of the straight channel and the winding channels are 38 lattices and 20 lattices, respectively. Finally, we compare the simulations with the μ-LIF experiments in a cross-shape microchannel with a computational domain consisting of 500 × 92 × 22 lattices, as shown in Figure 1b. The channel width (w) and the depth (H) are 20 lattices in both cases.

Results and Discussion

To determine the internal fluid movement in the moving droplets, we calculate the relative velocities in a coordinate system which is defined as moving at the same velocity as the droplet. All vectors in sections Validation of LBM simulation and Mixing patterns inside droplet through the 90°-winding channel represent velocities relative to the moving droplet, and the vectors in Sec. 4.4 represent velocities relative to the channel wall. The average velocity of the moving droplet is calculated as in Eqs. 18 and 19.

$$Q = \frac{1}{L_{\text{d}}} \int_0^L \left(\int_s U \cdot \boldsymbol{n} \boldsymbol{dS} \right) \boldsymbol{dl} \tag{18}$$

$$U_{\text{ave}} = \frac{Q}{S} \tag{19}$$

where L_{d} and S are the length and the cross-section of the droplet, respectively; U and U_{ave} are the local velocity vector and the average velocity of the droplet, respectively; $\boldsymbol{n}$ is the unit vector normal to the surface element $\boldsymbol{dS}$; and $\boldsymbol{l}$ is the streamwise coordinate.

In the microchannels, the viscous and interfacial forces are more important than the inertial effects and the gravity force. Their relative magnitude determines the fluid flow behaviors. Therefore, flows in the microchannel can be characterized by a group of parameters, such as the interfacial tension (γ), the inlet volumetric flow (Q_{c} and Q_{d}), the

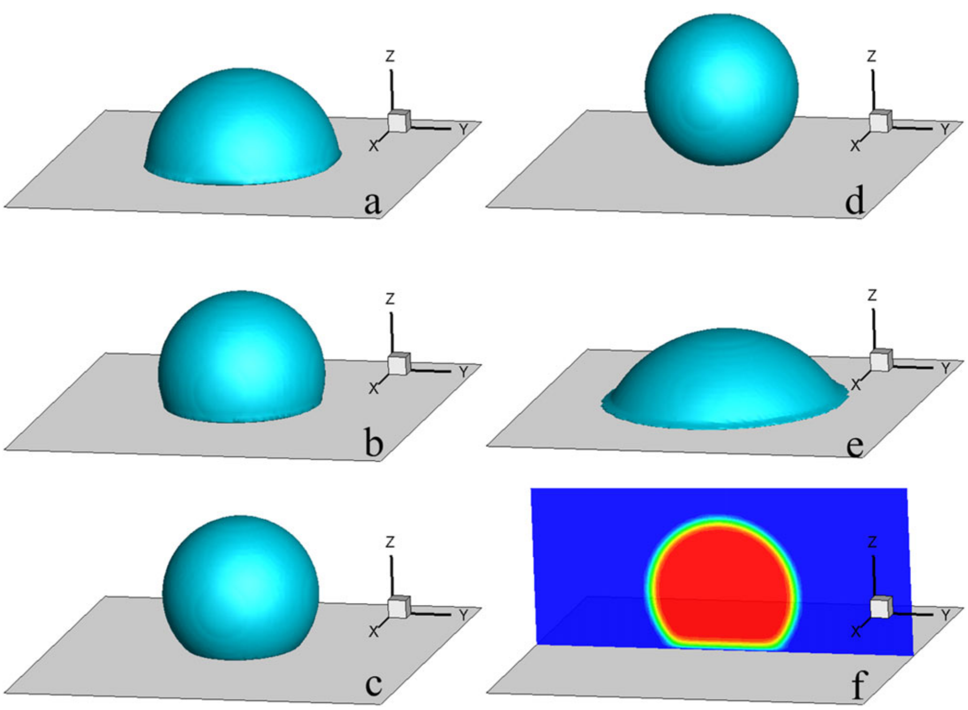

Figure 2. Different wettability of Fluid 2.

$G_{12} = 3$, $G_{1s} = 3$, (a) $G_{2s} = 0$; (b) $G_{2s} = 0.5$; (c) $= 1$; (d) $G_{2s} = 1.5$; (e) $G_{2s} = -0.5$; (f) $G_{2s} = 1$. [Color figure can be viewed in the online issue, which is available at wileyonlinelibrary.com.]

dynamic viscosity (μ_c and μ_d), and the wettability. The capillary number (Ca), which describes the relative importance of the viscosity and the interfacial tension, is the most important parameter to understand flow formation in such channels. The definition of Ca is given in Eq. 20

$$Ca = \frac{\mu_c u_c}{\gamma} \tag{20}$$

where u_c is the average inlet velocity of the continuous phase, μ_c the dynamic viscosity of the continuous phase, and γ the interfacial tension between the two phases. We use the subscripts c and d to refer to the continuous and dispersed phases, respectively.

Validation of LBM simulation

It should be mentioned that the LBM simulations are executed in the so-called lattice units. One can compare the LBM results with physical problems by comparing dimensionless groups, such as Ca numbers, Re numbers, and Q_d/Q_c. One lattice cell usually corresponds to 5 or 10 μm.[13,26,27] To validate the numerical method, a single-component flow was first modeled in a square-shaped geometry with periodic boundary. The kinematic viscosity of the fluid was set to be 0.167, and the overall pressure gradient parameter was set to be 8×10^{-5}. Under the given flow condition, the pressure difference (the density difference) in the entire channel was 1.59%, which meets the conditions for the incompressible fluids.

To obtain the relationship between the value of $G_{\sigma\bar{\sigma}}$ and the interfacial tension γ, a simple determination course was designed before carrying out the simulations. Here, a 3-D cube domain, containing 80 × 80 × 80 lattices, was first filled with Fluid 1. Then, different sizes of droplets of Fluid 2 were placed at the center of this domain. After achieving the equilibrium states (sufficient amount of computational steps is needed, always more than 50,000 steps), the pressures inside and outside the droplet were recorded. The Young–Laplace law was used to determine the interfacial force, as shown in Eq. 21

$$p_{in} - p_{out} = \frac{\gamma}{R} \tag{21}$$

where p_{in} and p_{out} are the pressure inside and outside the droplet, γ is the surface tension between the two phases, and R is the radius of the droplet. When $G_{\sigma\bar{\sigma}}$ is 2.6, 2.8, 3.0, 3.2, and 3.4, the nondimensional interfacial tension can be determined as 0.112, 0.120, 0.128, 0.144, and 0.160, respectively.

Each fluid component can interact with solids independently via separate interaction parameters. This is as expected considering that there are interfacial tension values between the two fluids (σ_{12}) and between each fluid and the surface (σ_{1s} and σ_{2s}) that appear in Young's equation

$$\cos\theta_d = \frac{\sigma_{2s} - \sigma_{1s}}{\sigma_{12}} \tag{22}$$

which determines the contact angle (θ_d) of Fluid 2 measured in Fluid 1.

Again, we used a 3-D square domain (containing 80 × 80 × 80 lattices) filled with Fluid 1. Then, 30 × 30 × 30 lattices of Fluid 2 were placed at the edge of this domain. We fixed the values of G_{12} and G_{1s}. We varied the value of G_{2s} to examine the wettability of two fluids. Figure 2 shows the wettability of Fluid 2 under different values of G_{2s}. The middle plane of the droplet was used to measure the contact angle of the fluid g, as show in Figure 2f. In our simulations, Component 1 was set as the continuous wetting phase,

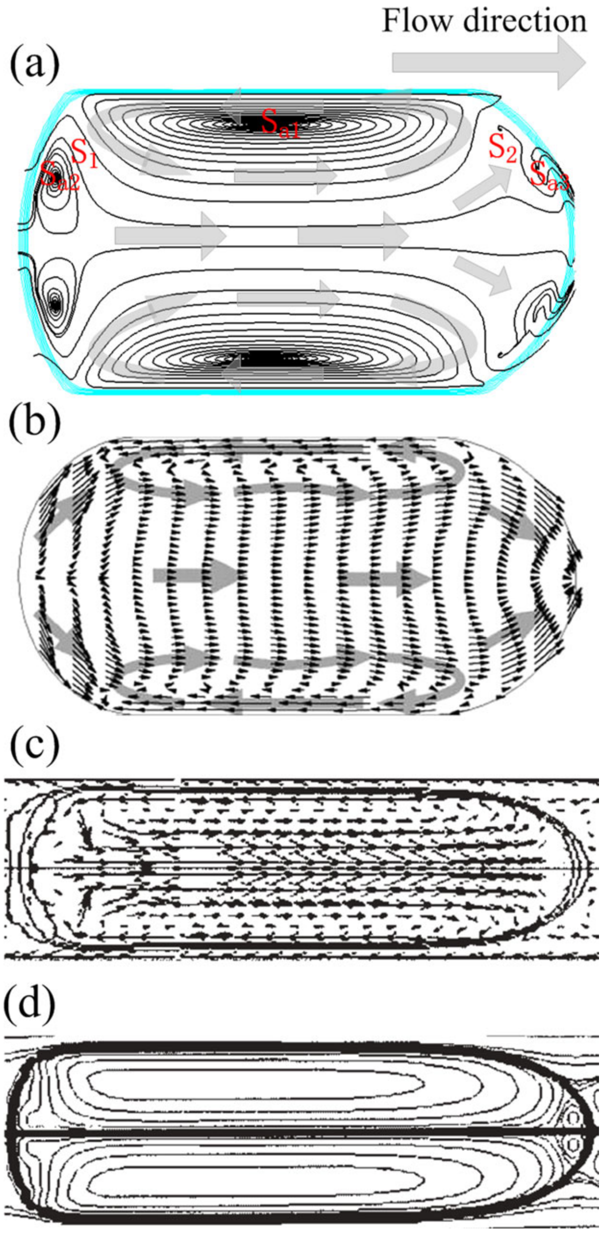

Figure 3. Velocity field inside droplet in microchannels.

(a) *xy*-plane from a 3-D simulation result; (b) *xy*plane from μ-PIV experiments[14]; (c) *xy*-plane from a 3-D simulation result[15]; (d) *xy*-plane from a 2-D simulation result.[15] [Color figure can be viewed in the online issue, which is available at wileyonlinelibrary.com.]

whereas Components 2 and 3 were the disperse nonwetting phase. It should be noticed that there are a maximum of two phases in our simulation, the disperse phase and the continuous phase. Components 2 and 3 are miscible with each other and immiscible with Component 1.

To validate the 3-D model, comparisons have been made with the experimental[14] and numerical[15] velocity field from the literature, as shown in Figure 3. In our simulation, the kinematic viscosity of the continuous flow was set to be 0.167, and the viscosity ratio of the fluid (μ_c/μ_d) was 0.5. The density ratio of the fluid (ρ_c/ρ_d) was 0.7. The nondimensional interfacial tension was 0.128. The contact angle of the Fluid 2 was 160°. The *Ca* number was around 0.022 and the *Re* number was around 2.5. Because all vectors in the figures represent velocities relative to the moving droplet, the velocity is oriented toward the front in the central region of the droplet, whereas in the vicinity of the sidewalls it is oriented toward the back of the droplet. This flow phenomenon generates a pair of vortices stretched along the moving direction near both sidewalls of the channel (as shown in Figures 3a, b, and c). In a (micro-)channel, the flow rate in the central region is higher than that near the wall, as the so-called Poiseuille flow. In the confined space like a droplet, however, the fluid inside the droplet cannot flow out of the droplet. The circulation is due to the difference of the fluid velocity from different positions inside the droplet, which leads to this flow topology inside the droplet. The main flow features in our simulation show good agreement with the experimental data by Haruyuki et al.[14] The vortices are symmetrically distributed on the two halves of the droplet through the moving direction, which enhance the mixing by circulation in each half and form some singular points (Figure 3a-S_{a1}, S_{a2}, S_{a3}, S_1, S_2). Because the fluid is incompressible and no source or sink is presented, there can be only two kinds of singular points: (1) saddles (unstable) at the meeting point between two opposite flowing streamlines or (2) centra (stable) in presence of a nonzero curl.[33] In each half of the droplet, there are three main singular points: S_{a1} determines the flow topology of the main vortex; S_{a2} and S_{a3} determine the small circulation zones in the anterior and posterior parts, which are caused by the interaction between the continuous phase and the dispersed phase. These three singular points form two saddles points (S_1 and S_2) at the meeting points between them. These small vortices were not revealed by Haruyuki's experiment, but Sarrazin et al.[15] has revealed this circulation zone by direct numerical simulations (as shown in Figure 3d). In our previous work,[27] we have also validated our model with different flow patterns in the microchannels and performed the quantitative comparison with both the experiment data and the simulation results in the literature.

Mixing patterns inside droplet through the 90°-winding channel

As has been shown in Figure 3, the droplet moving in the straight channel has a pair of vortices stretched along the moving direction near both sidewalls of the channel in the *xy*-plane (also in the *xz*-plane). Although these vortices can enhance the mixing of the fluid inside the dispersed flow, they are still separated by the middle axis of the droplet. In the straight channels, two symmetric vortices form on the left and right halves of a droplet (i.e., in the direction of the droplet movement). The mixing occurs by convection within each half and mainly takes place by diffusion between the two semispheres of the droplet. Some researchers have already indicated that mixing and/or chemical reactions in droplet-based microfluidic devices can be accelerated when the droplets are transported through a winding microchannel.[10]

Figure 4a shows the velocity field inside the droplet along the moving direction in the 90°-winding channel. The velocity gradients still determine the flow topology inside the droplet, but the flow phenomenon is more complex when the channel changes direction. Due to the change of the flow direction in the winding channel, the interaction between the backward flow from the side of the upstream and the forward flow from the center of the downstream creates a

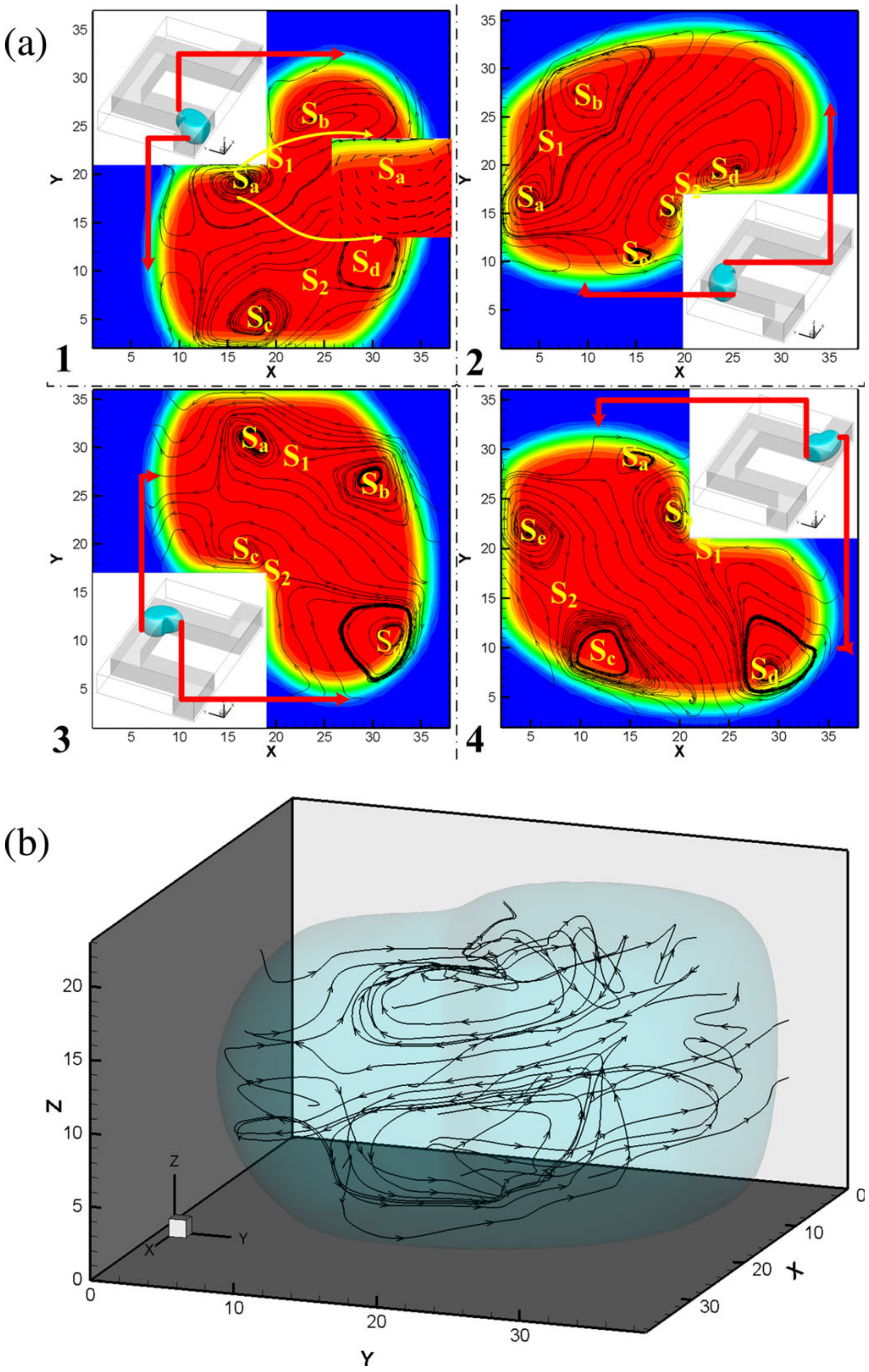

Figure 4. The streamlines inside the droplet in the 90°-winding channel.

(a) Streamlines at *xy* plane, $z = 11$: (1) at the first corner; (2) at the second corner; (3) at the third corner; (4) at the forth corner. (b) 3-D flow field. [Color figure can be viewed in the online issue, which is available at wileyonlinelibrary.com.]

vortex at the corner of the channel. The saddle points (Figure 4a-1-S_1, S_2) at the corner divide the original vortices along the sidewalls into two parts (Figure 4a-1-S_a and S_b, S_c, and S_d). With the droplet moving through the corner, a new vortex can be formed (Figure 4a-2-S_e, Figure 4a-4-S_e) at the posterior part of the droplet, and S_d may move to the anterior part of the droplet (Figure 4a-3, 4). The formation and the movement of the vortices enable the convection of the flow at the different sides of the middle axis, which makes up for the weakness of the straight channel. The streamlines in Figure 4a are actually the projection of these 3-D flow fields on the 2-D plane. Figure 4b shows a 3-D

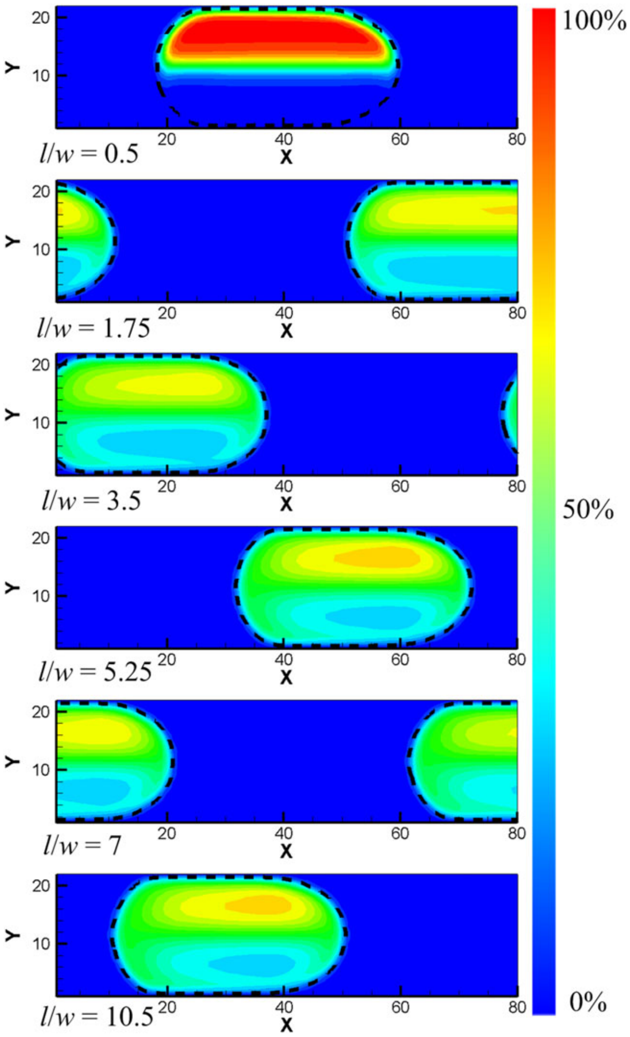

Figure 5. LBM simulations of mixing behavior inside the droplet in the straight channel.

$\mu_c/\mu_d = 0.5$, $\theta_d = 160°$, $Ca = 0.022$. $G_{12} = 3$, $G_{13} = 3$, $G_{23} = 1.6$. Color represents the normalized concentration of Component 2, where the pure red denotes 100% Component 2 and the pure blue denotes 0%. [Color figure can be viewed in the online issue, which is available at wileyonlinelibrary.com.]

vision of the streamlines inside the droplet in the winding channel. We can see clearly that 3-D flow fields are more complex than the 2-D flow fields; there are two main vortexes inside the droplet in 3-D and some small vortexes in the local droplet. The 3-D effects of velocity gradients together with the change of the flow direction determine the complex flow topology inside the droplet. With the movement of the droplet passing through the corner, the vortices reorient the fluid inside the droplet and thereby accelerate the mixing. After several turns, the fluid inside the droplet can achieve a well-mixed state. The effect of this acceleration is related to the winding angle of each turning corner. A larger angle can make the internal circulation more intense, but it will increase the flow resistance and the manufacturing difficulty.

Microfluidics with three fluid components are used for a direct understanding of the mixing process, as shown in Figures 5 and 6. The flow conditions are the same as mentioned in Validation of LBM simulation Fluid 1 serves as the continuous phase, Fluids 2 and 3 serve as the dispersed phases to be mixed. Colors represent the normalized concentration of Fluid 2: pure red denotes 100% Liquid 2 and pure blue denotes 0%.

As can be seen in Figures 5 and 6, the 90°-winding channel can significantly intensify the mixing performance inside microdroplets. In the straight microchannels, Taylor flow exists with a circulation flow pattern for the wall effect in microchannels. The droplet has a pair of vortices stretched along the moving direction near both sidewalls of the channel in the *xy* plane (i.e., the horizontal plane) Within each half-sphere, the mixing occurs by convection. Between them, it mainly takes place by diffusion as it is a laminar flow in a straight microchannel. The winding channel can reorient the fluid inside the droplet, causing recirculation inside, which could enhance the mixing in microfluidic devices. Song et al.[10] assumes that this acceleration is due to the fluid movements, such as circulations or vortices generated by the droplet handling through their experiments. This study has proven this flow mechanism of a moving droplet in a winding channel through a numerical simulation by using the 3-D multicomponents LB model.

Mixing performances of microdroplets for different channel designs

To quantitatively analyze the mixing process, intensity of segregation (IOS) is used to characterize the mixing performance. The parameter IOS is a measure of the difference of concentration between pure liquids with and without tracer.[34] The IOS can be calculated from the normalized concentration inside the whole droplet. The IOS is defined as

$$C = \frac{C_2}{C_2 + C_3} \tag{23}$$

$$\mathrm{IOS} = \frac{\sigma_C^2}{<C> \cdot (1 - <C>)} \tag{24}$$

where C is the percentage composition of the mixture in terms of Component 2 (Fluid 2) at each individual measurement pixel, $<C>$ is the mean concentration of Component 2 inside the whole droplet, and σ_C is the standard deviation of $<C>$. IOS represents the extent to which the concentration in different regions in the mixing field departs from the mean value: a value of 1 for IOS corresponds to a totally segregated system, whereas a value of 0 corresponds to a homogeneous mixture.

As mentioned in Multicomponent LB model, we can change the diffusion rate between the miscible components by adjusting the relative value of $G_{\sigma\bar{\sigma}}$. Figure 7 shows a quantitative comparison of mixing performance between two channels under different diffusion parameters. It can be seen that there are two stages in the mixing process in the straight channel. For a better understanding, we define the red region in Figure 5 ($l/w = 0.5$) as part-a with Component 2 (Fluid 2) in it at the very beginning of the mixing process, and the other region inside the droplet as part-b with Component 3 (Fluid 3) in it. In the initial stage, the concentrations of Components 2 and 3 in parts a and b are very different. The diffusion rate is relatively fast near the middle axis of the droplet. Component 3 diffuses fast from part-b into part-a through the middle axis, and spreads quickly inside part-a thanks to the vortex in this half-sphere, leading to a relatively fast decline of IOS value inside the droplet. With different diffusion rate, the mixing efficiency is also very

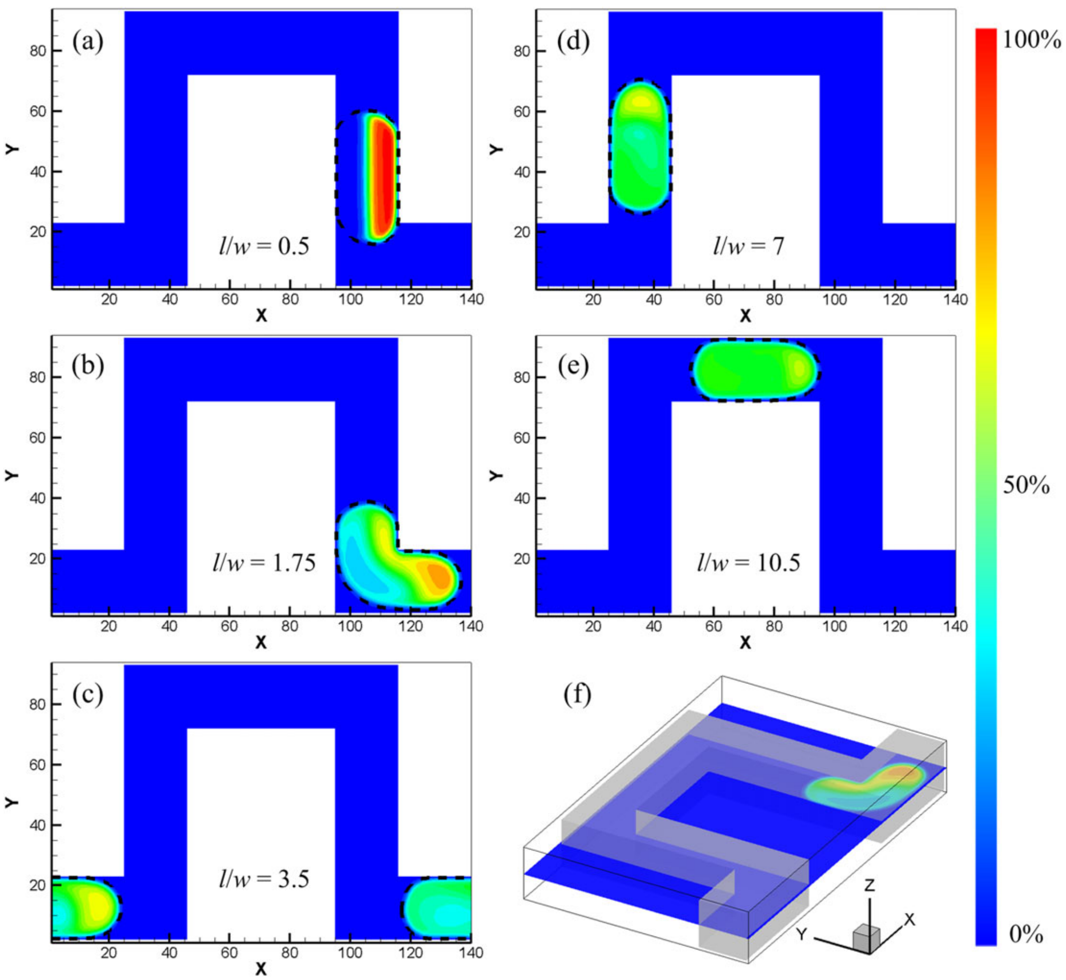

Figure 6. LBM simulations of mixing behavior inside the droplet in the 90°-winding channel.

$\mu_c/\mu_d = 0.5$, $\theta_d = 160°$, $Ca = 0.022$. $G_{12} = 3$, $G_{13} = 3$, $G_{23} = 1.6$. Color represents the normalized concentration of Component 2, where the pure red denotes 100% Component 2 and the pure blue denotes 0%. $\mu_c/\mu_d = 0.5$, $\theta_d = 160°$, $Ca = 0.022$. $G_{12} = 3$, $G_{13} = 3$, $G_{23} = 1.6$. Color represents the normalized concentration of Component 2, where the pure red denotes 100% Component 2 and the pure blue denotes 0%. [Color figure can be viewed in the online issue, which is available at wileyonlinelibrary.com.]

different during this stage. During the latter stage, the concentration difference near the middle axis becomes small, and the mixing speed slows down in the straight channel. In the winding channel, the fluid inside the droplet is reoriented because of the sudden change of the direction of the droplet, which results in more effective mixing by recirculation flows. When the interaction is weak, the diffusion speed is relatively fast and the effect of the channel geometry is not obvious. When the diffusion speed is relatively slow, the effect of fluid reorientation is obvious and results in more effective mixing by recirculation flows. The effect of the winding channel is to break the symmetric distribution of the fluids inside the droplet, leading to an effective mixing inside the droplet.

To further investigate the winding effect, we simulate the processes of four channels with different winding shapes: straight channel, 45–135° channel, 90° channel, and Z channel. Figure 8 shows typical results for these four different channels. Although the plug passes through the turning corner, the vortices at the corner reorient the fluid inside the plug to different extents according to the winding designs. But as long as the symmetric distribution of the fluid is periodically broken in a relatively large corner, it can notably intensify the circulation in each half of the droplet thereby

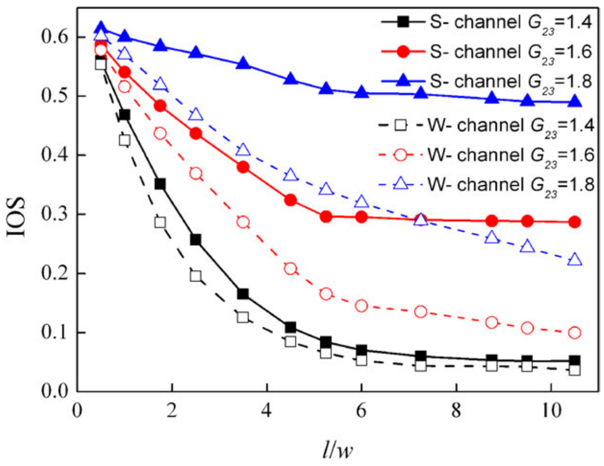

Figure 7. Comparison of mixing performance using IOS along the flow direction between straight and 90°-winding channels for different G_{23}.

[Color figure can be viewed in the online issue, which is available at wileyonlinelibrary.com.]

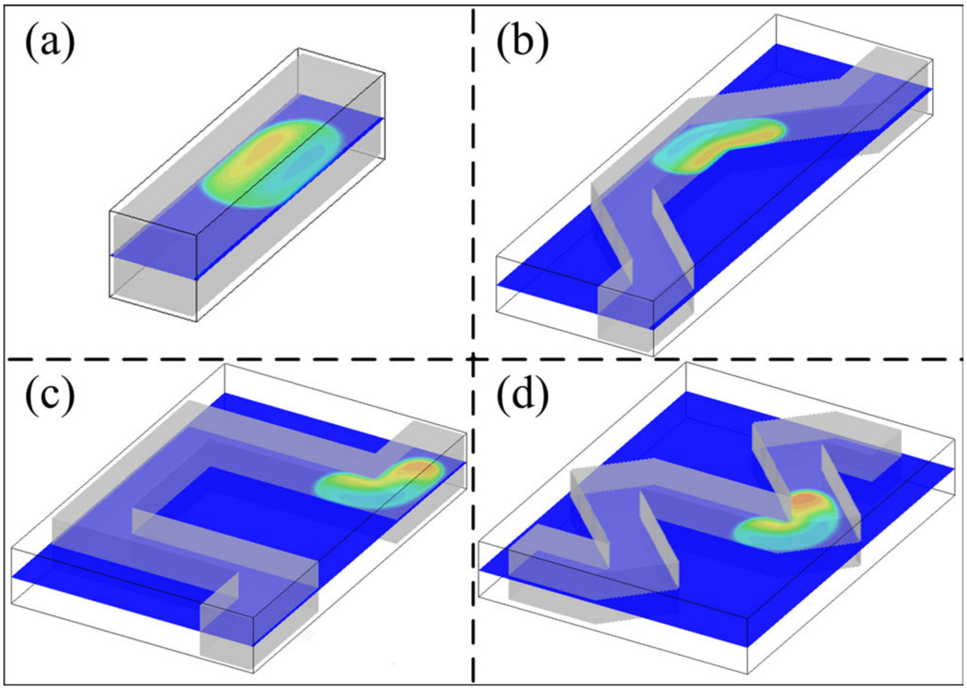

Figure 8. LBM simulations of mixing behavior inside the droplet in different channels.

$\mu_c/\mu_d = 0.5$, $\theta_d = 160°$, $Ca = 0.022$. $G_{12} = 3$, $G_{13} = 3$, $G_{23} = 1.6$. Color represents the normalized concentration of Component 2, where the pure red denotes 100% Component 2 and the pure blue denotes 0%. (a) straight channel; (b) 45–135° winding channel; (b) 90° winding channel; (d) Z winding channel. [Color figure can be viewed in the online issue, which is available at wileyonlinelibrary.com.]

accelerating the mixing performance inside the droplet. Figure 9 shows a quantitative comparison of the mixing performance through the channels. It is interesting to notice that, under the typical simulation conditions, the effect of mixing intensification is almost independent of the winding angle of the corner, which indicates that the angle can be adjusted flexibly according to the specific need of the production process.

Mixing performance considering the droplet generation

In the work aforementioned, we have considered the mixing behaviors inside droplets for fully developed situations in the experiments corresponding to the simulation results using periodic boundary conditions. In this section, we pay attention to the full process starting from the droplet formation in a cross-shaped microchannel design (shown in Figure 1b). μ-LIF experiments were carried out to validate our simulation results.

In both experiments and simulations, Fluid 1 served as the continuous phase, Fluids 2 and 3 served as the dispersed phases to be mixed. The flow conditions were the same as

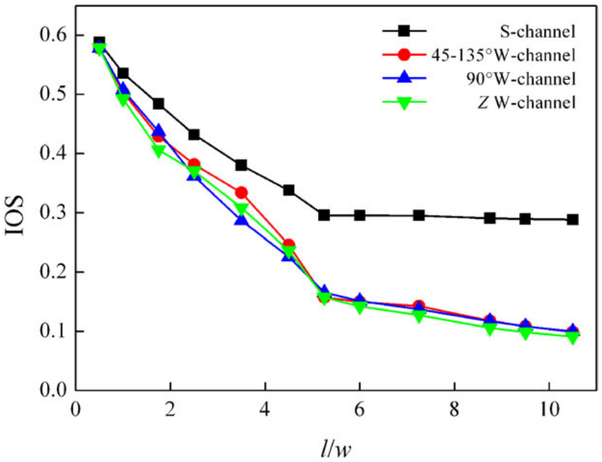

Figure 9. Comparison of mixing performance using IOS along the flow direction between straight and winding channels.

[Color figure can be viewed in the online issue, which is available at wileyonlinelibrary.com.]

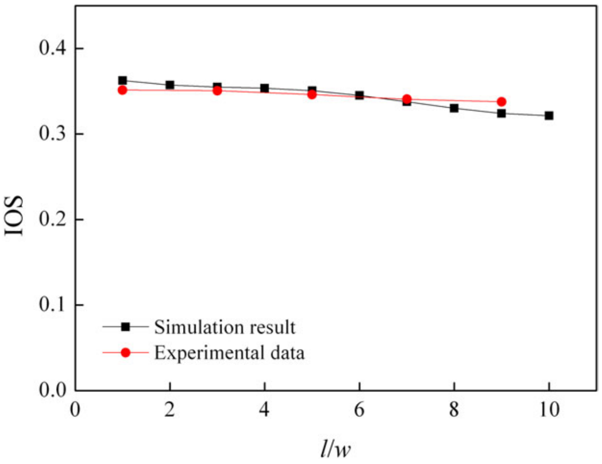

Figure 10. Comparison of the simulation results and experimental data in terms of IOS inside the droplets.

$\mu_c/\mu_d = 0.5$, $\theta_d = 160°$, $Ca = 0.026$, $D/w = 2.5$. $Qc = 0.2$ (simulation), $Q_d = 0.02$ (simulation), $Q_c = 92.5$ μL min^{-1} (experiment), $Q_c = 9.25$ μL min^{-1} (experiment). [Color figure can be viewed in the online issue, which is available at wileyonlinelibrary.com.]

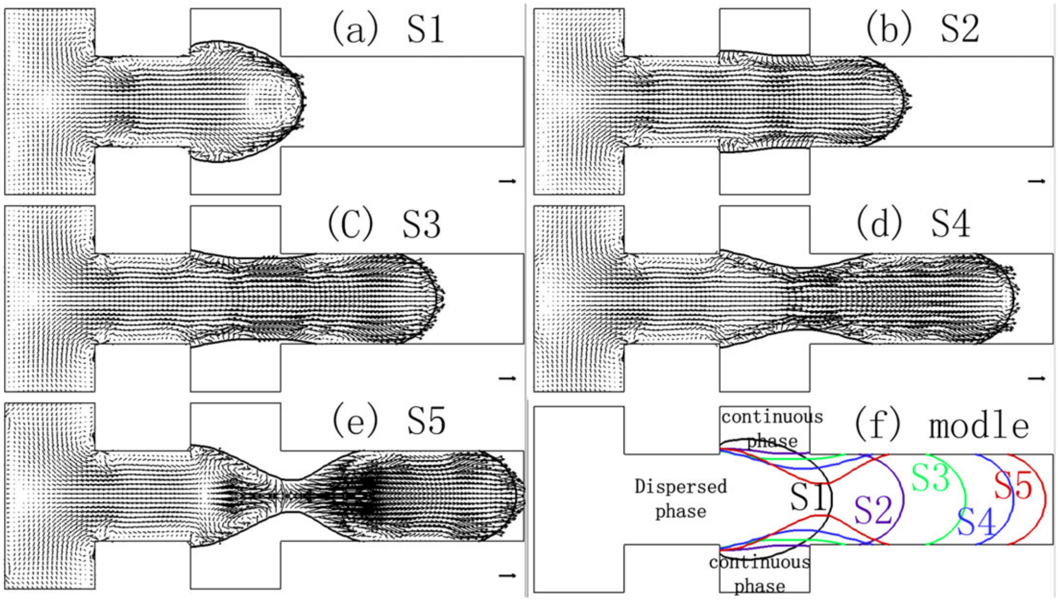

Figure 11. Local flow fields during the process of droplet generation in the cross-shaped microchannel.

Simulation result, $Ca = 0.026$, $Q_c = 0.2$, $Q_d = 0.02$. [Color figure can be viewed in the online issue, which is available at wileyonlinelibrary.com.]

mentioned in Validation of LBM simulation. The Schmidt number ($Sc = \nu/D_{AB}$) is 10^3 inside the droplet, which shows that the mixing performance is significantly influenced by the flow field inside the droplet. Figure 10 shows the comparison of the IOS value obtained by simulation and experiments. It can be seen that the initial IOS value in the droplet

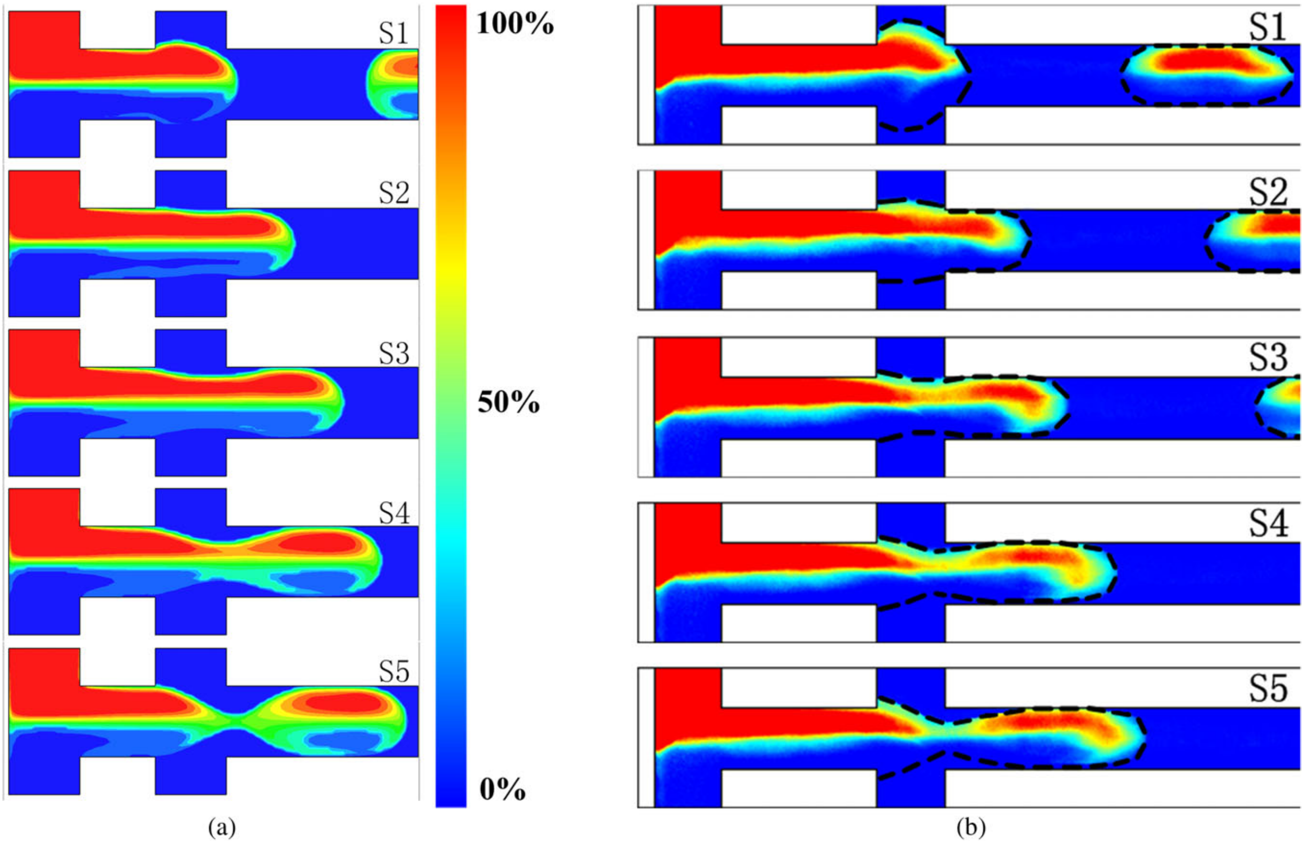

Figure 12. Mixing behaviors inside the droplet through the cross-shaped microchannel.

Color represents the normalized concentration of Component 2, where the pure red denotes 100% Component 2 and the pure blue denotes 0%. (a) Simulation, $Ca = 0.026$, $Q_c = 0.2$, $Q_d = 0.02$. (b) Experiment, $Ca = 0.026$, $Q_c = 92.5$ μL min^{-1}, $Q_d = 9.25$ μL min^{-1}. [Color figure can be viewed in the online issue, which is available at wileyonlinelibrary.com.]

is relatively low and declines slowly in the latter straight channels. Our simulation results have good concordance with experimental data in terms of the mixing extent inside the whole droplet.

Figure 11 gives the local flow fields inside the droplet in xy-plane during the process of droplet generation in a cross-shaped channel. We split the process into five stages (S1–S5), as shown in Figure 11f. Because of the symmetry of the channel geometry, the velocities of the two fluids in the dispersed phase are the same everywhere, and they flow symmetrically into the droplet in every stage including the droplet generating process. In the channel, the droplet is formed by the flow focusing method of the continuous phase. Due to the extrusion effect of the continuous phase, internal circulations at the head and the tail of the droplet are formed (see Figure 11-S1–S5), which can intensify the local mixing performance inside the droplet. Figures 12a (simulation) and b (experiment) clearly illustrate the mixing behaviors in a cross-shaped channel. The simulation results in this geometry agree well with the experiment data. It can be seen from these two figures that the circulation in the anterior and posterior parts of the droplet enhances the local mixing quality, but the fluids distribute symmetrically on each side of the droplet. Therefore, in the following movement after the detachment of the droplet, the IOS of the droplet generated from the cross channel has a relatively low initial value with a slow declining trend. It is to be noticed that the process of droplet generation determines the initial liquid distribution inside the droplet, and that different droplet generation methods may have strong influence on the mixing performance inside the droplet along its movement in a channel. For different microfluidic configurations, the basic principles in terms of physics do not change. Standing on the validation foundation in a cross-shaped microchannel, we think that the modeling approach can be further used to predict the fluid dynamics and mixing in other configurations. Future work will focus on investigating the mixing performance as well as the process intensification during the droplet generation.

Conclusions

For a thorough understanding on the complex hydrodynamics inside microdroplets, a 3-D multicomponents LB model has been established and then applied to simulate droplet flows in microchannels. The 3-D hydrodynamics of the liquid-liquid flow are obtained with detailed information of the mixing performance inside microdroplets. The simulation results show good consistency with our μ-LIF measurements and the available work in the literature. In a straight channel, mixing occurs by convection in two symmetric vortices and mainly by diffusion between them. Whereas in a winding channel, the fluid inside the droplet is reoriented because of the quick change in the droplet direction, which results in more effective mixing by recirculation flows. This recirculation phenomenon inside the droplet could enhance the mixing and the chemical reactions in microfluidic devices. It is interesting to see that the effect of this acceleration is almost independent of the winding angle at the corner as long as the angle is large enough to break the flow symmetry inside the droplet, that is, to reorient the fluid movement. In this sense, the flow mechanism and the mixing performance inside the droplet in droplet-based microfluidics have been revealed in this work, which should be helpful for the microdevice design and optimization.

Acknowledgments

Financial supports from National Natural Science Foundation of China (No. 20776074 & 20906057) and Specialized Research Fund for the Doctoral Program of Higher Education (No. 20090002110069) are acknowledged. This work is also under the support of Key Lab for Industrial Biocatalysis, Ministry of Education, China.

Notation

C = normalized concentration of the species
Ca = Capillary number
f = probability density functions of fluid σ
F = interaction force, lattice units
G = interaction strength, lattice units
H = channel height, m (in experiment) and lattice units (in simulation)
IOS = intensity of segregation
l = flow distance along the flow direction, m (in experiment) and lattice units (in simulation)
Q = volumetric flow rate, m^3/s (in experiment) and lattice units (in simulation)
p = pressure, Pa (in experiment) and lattice units (in simulation)
u = velocity, m/s (in experiment) and lattice units (in simulation)
S = singular point
S-channel = straight channel
W = channel width, m (in experiment) and lattice units (in simulation)
W-channel = winding channel

Greek letters

γ = interfacial tension, N/m (in experiment) and lattice units (in simulation)
μ = dynamic viscosity, Pa·s (in experiment) and lattice units (in simulation)
v = kinematics viscosity, m^2/s (in experiment) and lattice units (in simulation)
θ = contact angle
ρ = density, kg/m^3 (in experiment) and lattice units (in simulation)
σ = index for fluid components
τ = relaxation time
ω = weighting coefficient
Ψ = interaction potential
Γ_1 = the local coefficient related to the experimental parameters
Γ_2 = the coefficient that takes into account the effect of absorption

Superscripts and subscripts

c = continuous phase
d = disperse phase
σ = fluid σ (σ = 1, 2, 3)
i = lattice direction
P = fluid components (particles)
S = solid surface

Literature Cited

1. He M, Edgar JS, Jeffries GDM, Lorenz RM, Shelby JP, Chiu DT. Selective encapsulation of single cells and subcellular organelles into picoliter- and femtoliter-volume droplets. *Anal Chem.* 2005;77:1539–1544.
2. Chen DL, Gerdts CJ, Ismagilov RF. Using microfluidics to observe the effect of mixing on nucleation of protein crystals. *J Am Chem Soc.* 2005;127:9672–9673.
3. Song H, Ismagilov RF. Millisecond kinetics on a microfluidic chip using nanoliters of reagents. *J Am Chem Soc.* 2003;125:14613–14619.
4. Griffiths AD, Tawfik DS. Miniaturising the laboratory in emulsion droplets. *Trends Biotechnol.* 2006;24:395–402.
5. Song H, Chen DL, Ismagilov RF. Reactions in droplets in mcrofluidic channels. *Angew Chem Int Ed.* 2006;45:7336–7356.

6. Stroock AD, Dertinger SKW, Ajdari A. Chaotic mixer for microchannels. *Science.* 2002;295:647–651.
7. Mengeaud V, Josserand J, Girault HH. Mixing processes in a zigzag microchannel: finite element simulations and optical study. *Anal Chem.* 2002;74:4279–4286.
8. Wang HZ, Iovenitti P, Harvey E. Optimizing layout of obstacles for enhanced mixing m microchannels. *Smart Mater Struct.* 2002;11:662–667.
9. Hsieh SS, Huang YC. Passive mixing in microchannels with geometric variations through mu PIV and mu LIF measurements. *J Micromech Microeng.* 2008;18:065017–065027.
10. Song H, Bringer MR, Tice JD, Gerdts CJ, Ismagilov RF. Experimental test of scaling of mixing by chaotic advection in droplets moving through microfluidic channels. *Appl Phys Lett.* 2003;83:4664–4666.
11. Brian KHY, Axel G, Martin AS, Klavs FJ, Moungi GB. A microfabricated gas-liquid segmented flow reactor for high-temperature synthesis: the case of CdSe quantum dots. *Angew Chem Int Ed.* 2005;44:5447–5451.
12. Liu Z, Huang YB, Jin Y, Cheng Y. Mixing intensification by chaotic advection inside droplets for controlled nanoparticle preparation. *Microfluid Nanofluid.* 2010;9:773–786.
13. Yu Z, Hemminger O, Fan LS. Experiment and lattice Boltzmann simulation of two-phase gas-liquid flows in microchannels. *Chem Eng Sci.* 2007;62:7172–7183.
14. Haruyuki K, Shohei K, Teruo F, Marie O. Three-dimensional measurement and visualization of internal flow of a moving droplet using confocal micro-PIV. *Lab Chip.* 2007;7:338–346.
15. Sarrazin F, Loubière K, Prat L, Gourdon C, Bonometti T, Magnaudet J. Experimental and numerical study of droplets hydrodynamics in microchannels. *AIChE J.* 2006;52:4061–4070.
16. Raimondi ND, Prat L. Numerical study of the coupling between reaction and mass transfer for liquid-liquid slug flow in square microchannels. *AIChE J.* 2011;57:1719–1732.
17. Shan XW, Chen HD. Lattice Boltzmann model for simulating flows with multiple phases and components. *Phys Rev E.* 1993;47:1815–1819.
18. Lin H, Chao CH, Wei CW. Low azeotropic solvent for bonding of PMMA microfluidic devices. *Sens Actuators B.* 2007;121:698–705.
19. Guillard F, Fritzon R, Revstedt J, Tragardh C, Alden M, Fuchs L. Mixing in a confined turbulent impinging jet using planar laser-induced fluorescence. *Exp Fluids.* 1998;25:143–150.
20. Houcine I, Vivier H, Plasari E, David R, Villermaux J. Planar laser induced fluorescence technique for measurements of concentration fields in continuous stirred tank reactors. *Exp Fluids.* 1996;22:95–102.
21. Liu Z, Cheng Y, Jin Y. Fast liquid jet mixing in millimeter channels with various multislits designs. *Ind Eng Chem Res.* 2008;47:9744–9753.
22. Wang WT, Zhao SF, Shao T, Jin Y, Cheng Y. Visualization of micro-scale mixing in miscible liquids using μ-LIF technique and drug nano-particle preparation in T-shaped microchannels. *Chem Eng J.* 2012;192:252–261.
23. Gunstensen AK, Rothman DH, Zaleski S, Zanetti G. Lattice Boltzmann model of immiscible fluids. *Phys Rev A.* 1991;43:4320–4327.
24. Swift MR, Osborne W, Yeomans JM. Lattice Boltzmann simulation of nonideal fluids. *Phys Rev Lett.* 1995;75:830–833.
25. Gupta A, Kumar R. Effect of geometry on droplet formation in the squeezing regime in a microfluidic T-junction. *Microfluid Nanofluid.* 2010;8:799–812.
26. van der Graaf S, Nisisako T, Schroën CGPH, van der Sman RGM, Boom RM. Lattice Boltzmann simulations of droplet formation in a T-shaped microchannel. *Langmuir.* 2006;22:4144–4152.
27. Wang WT, Liu Z, Jin Y, Cheng Y. LBM simulation of droplet formation in microchannels. *Chem Eng J.* 2011;173:828–836.
28. Succi S, d'Humières D, Qian Y, Orszag SA. On the small-scale dynamical behavior of lattice BGK and lattice Boltzmann schemes. *J Sci Comput.* 1993;8:219–230.
29. Shan XW, Doolen G. Multicomponent lattice-Boltzmann model with interparticle interaction. *J Stat Phys.* 1995;81:379–393.
30. Chen S, Martínez D, Mei R. On boundary conditions in lattice Boltzmann methods. *Phys Fluids.* 1996;8:2527–2536.
31. Zou QS, He XY. On pressure and velocity boundary conditions for the lattice Boltzmann BGK model. *Phys Fluids.* 1997;9:1591–1598.
32. Zhang J, Kwok DY. Pressure boundary condition of the lattice Boltzmann method for fully developed periodic flows. *Phys Rev E.* 2006;73:047702 (4).
33. Volpe G, Volpe G, Petrov D. Singular-point characterization in microscopic flows. *Phys Rev E.* 2008;77:037301 (4).
34. Danckwerts PV. The definition and measurement of some characteristics of mixtures. *Appl Sci Res.* 1952;3:279–296.

Manuscript received Nov. 28, 2011, and revision received Sep. 26, 2012.